Eur. Phys. J. Plus (2020) 135:409
https://doi.org/10.1140/epjp/s13360-020-00428-2

THE EUROPEAN PHYSICAL JOURNAL PLUS

Regular Article

A multiphysics model for analysis of inert gas bubbles in Molten Salt Fast Reactor

Parikshit Bajpai, Stefano Lorenzi, Antonio Cammi[a]

Department of Energy, Nuclear Engineering Division, Politecnico di Milano, Via La Masa 34, 20156 Milan, Italy

Received: 29 May 2019 / Accepted: 29 April 2020

Abstract Molten salt reactors (MSRs) have gained worldwide interest in recent years due to their appealing safety and resource utilisation characteristics. These reactors have a unique feature, i.e. the presence of nuclear fuel in the form of a molten fluoride or chloride salt containing the fissile and fertile materials. The fuel salt also acts as the coolant, and this dual role results in a complex, highly coupled multiphysics system which poses a challenge in modelling and simulation of MSRs. This paper presents the development of a simulation model for the Molten Salt Fast Reactor (MSFR) to predict the behaviour of inert gas bubbles in the core and to quantify their impact on the reactivity. Inert gas bubbles in MSFR have been modelled using a multiphysics approach coupling computational fluid dynamics for fluid flow and heat transfer with neutron diffusion equation for neutronics and a balance equation with diffusion and advection terms for taking into account the drift of the delayed neutron precursors. The two-phase flow has been modelled using a simplified Euler–Euler model for small volume fraction of the dispersed phase, i.e. for small bubble fraction, which combines the momentum and continuity equation of the liquid and gas phases and adds a gas-phase transport equation to track the void fraction. Simulations reveal that the bubble distribution in the core has a significant impact on reactivity resulting in a difference in the bubbling feedback coefficient compared to studies using a homogeneous distribution.

1 Introduction

The Molten Salt Fast Reactor (MSFR) is the reference circulating-fuel reactor selected under the framework of Generation-IV International Forum. This reactor concept was initially studied under the EURATOM EVOL project and was subsequently developed under the HORIZON-2020 SAMOFAR project [1,2]. In MSRs, a molten fluoride salt acts as both the fuel and coolant. While this peculiar feature offers several advantages over solid-fuelled reactors, it also poses a challenge in terms of reactor design and modelling. In MSFR, the velocity field has a significant impact on the distribution of the delayed neutron precursors (DNPs), thus affecting the reactor kinetics and resulting in a tightly coupled multiphysics problem [3].

Focus Point on Advances in the physics and thermohydraulics of nuclear reactors edited by J. Ongena, P. Ravetto, M. Ripani, P. Saracco.

[a] e-mail: antonio.cammi@polimi.it (corresponding author)

Published online: 19 May 2020

Moreover, a bubbling system has been proposed in the MSFR design for online removal of fission products. In addition to its primary objective, bubble injection can also be seen as a reactivity control method by exploiting the highly negative void feedback coefficient in MSFR [2]. However, such an application requires development of a multiphysics model capable of evaluating the impact of bubbles on the thermal hydraulics and neutronics of MSFR. At present, most of the models available in the literature approximate the two-phase mixture of fuel salt and gas bubbles as a single-phase flow by including the void feedback effect in the density feedback. However, as the spatial distribution of the bubbles is expected to impact the void feedback, such a modelling approach is not suitable for the case of evaluating the feasibility of bubbling as a method of reactivity control. Moreover, while the density feedback mechanism is an intrinsic property of fuel salt, essentially related to fuel expansion with change in temperature, void feedback is endogenously related to the decrease in localised fuel concentration by insertion of bubbles. Therefore, to accurately predict thermal hydraulic and neutronic influence of gas bubbles, the bubbling system of MSFR must be modelled as a focussed subsystem.

To model the two-phase flow in MSFR, a two-fluid Euler–Euler approach has been proposed by Cervi et al. [4,5]. In these works, the authors have used this approach to evaluate the void reactivity feedback coefficient on the basis of spatial distribution of bubbles and have pointed out the differences with respect to simulations carried out with uniform void fractions. The adoption of this modelling approach can be computationally expensive and is often not worth the effort especially if the bubble fraction in the reactor is small. In such cases, a simplified formulation of the two-fluid model can be used with the aim of reducing the computational expenses through the application of efficient solutions strategies used for single-phase flows [6]. In this formulation, hereafter referred to as the *bubbly flow model*, a single equation representative of both the phases is used and the effect of the gas phase is accounted using a *gas-phase transport equation*. In this work, the bubbly flow model has been adopted to represent the dispersed flow of inert gas–fuel salt mixture. By coupling the bubbly flow model with heat transfer and neutronics, a multiphysics model has been developed and implemented using COMSOL Multiphysics to predict the impact of the aforementioned inert gas bubbles on reactivity of MSFR.

The paper is organised as follows. In Sect. 2, the mathematical equations used to describe the fluid flow have been presented and are followed by a brief discussion of the COMSOL Multiphysics implementation in Sect. 3. In Sect. 4, the results of the steady-state simulations and comparison with previous studies have been presented.

2 Description of the multiphysics modelling

2.1 Two-phase flow

Traditionally, two-phase flows have been classified into three main classes based on geometry of the interfaces, namely separated flows, mixed or transitional flows and dispersed flows, and the three classes of flow can be subdivided into different regimes [7,8]. The existence of flow in a particular regime is determined by the geometry of the system and the thermophysical properties of the phases, such as viscosity and surface tension, and these flow regimes strongly affect the interfacial exchanges of mass, momentum and energy. In the MSFR, bubbly flow regime is foreseen considering the discrete phase of gas bubbles immersed in the fuel salt which acts as the continuous phase.

Two-phase flows are traditionally modelled using two main approaches—the Eulerian—Lagrangian and the Eulerian–Eulerian approach. The Eulerian–Lagrangian approaches track the individual bubbles or clusters of bubbles through the carrier liquid by solving an appropriate equation of motion, while the Eulerian–Eulerian approaches describe the motion of bubbles in a macroscopic sense by taking phase ensemble averages of the microscopic flow equations [9]. In the two-fluid Euler–Euler framework, each phase (controlled by its own conservation equations which include the phase interaction terms) moves and develops independently. Several correlations appear in the model to account for loss of information associated with the averaging and additional closure relations must be added. This model, however, suffers from a loss of characteristics of the interfaces. This loss of topological information is not a shortcoming for application to the present work, since an averaged description of the two-phase flow is sufficient to predict the impact of bubbles on fluid flow and subsequently on neutronics. In addition, the better computational efficiency compared to Lagrangian particle tracking and the predictive capabilities of this approach makes it the preferred choice in the present work.

2.1.1 Two-fluid model

In the present state of the art, the Euler–Euler two-fluid model can be considered as the most detailed and accurate macroscopic formulation of the thermal hydraulics of two-phase flow systems. The model is expressed in terms of two sets of conservation equations governing the balance of mass, momentum and energy in each phase. The degree of coupling between the phases is decided by the interfacial interaction terms which, therefore, have a strong influence on the transfer processes. The transfer processes of each phase can be expressed by their own equations and, without the interfacial exchanges, the two phases are essentially independent.

As a starting point of the derivation of the simplified bubbly flow model, the Euler–Euler model employed by Cervi et al. [4] is presented since this model turned out to perform well in the description of the MSFR bubbling system. The Eulerian modelling framework is based on ensemble-averaged mass, momentum and energy balance equations for each phase. The Navier–Stokes equations are averaged for each phase over a volume that is small compared to the computational domain but large compared to the dispersed phase. The two phases are assumed to behave as two continuous and interpenetrating fluids. With the liquid phase as continuum and the gaseous phase (bubbles) as dispersed phase, the equations in non-conservative form [10,11] are presented in the following paragraphs.

The momentum equations can be written as the following:

$$\begin{aligned}\frac{\partial \rho_{\mathrm{l}}\alpha_{\mathrm{l}}\boldsymbol{u_l}}{\partial t} + \rho_{\mathrm{l}}\alpha_{\mathrm{l}}\boldsymbol{u_l}\nabla\cdot(\boldsymbol{u_l}) &= -\alpha_{\mathrm{l}}\nabla p + \alpha_{\mathrm{l}}\rho_{\mathrm{l}}\boldsymbol{g} + \nabla\cdot\alpha_{\mathrm{l}}(\tau_{\mathrm{l}} + \tau_{\mathrm{l}}^{\mathrm{T}}) + (\Gamma_{\mathrm{lg}}\boldsymbol{u_g} - \Gamma_{\mathrm{gl}}\boldsymbol{u_l}) \\ &\quad + \boldsymbol{M_{lg}} + \alpha_{\mathrm{l}}\boldsymbol{F_{V,l}} \\ \frac{\partial \rho_{\mathrm{g}}\alpha_{\mathrm{g}}\boldsymbol{u_g}}{\partial t} + \rho_{\mathrm{g}}\alpha_{\mathrm{g}}\boldsymbol{u_g}\nabla\cdot(\boldsymbol{u_g}) &= -\alpha_{\mathrm{g}}\nabla p + \alpha_{\mathrm{g}}\rho_{\mathrm{g}}\boldsymbol{g} + \nabla\cdot\alpha_{\mathrm{g}}(\tau_{\mathrm{g}} + \tau_{\mathrm{g}}^{\mathrm{T}}) + (\Gamma_{\mathrm{gl}}\boldsymbol{u_l} - \Gamma_{\mathrm{lg}}\boldsymbol{u_g}) \\ &\quad + \boldsymbol{M_{gl}} + \alpha_{\mathrm{g}}\boldsymbol{F_{V,g}}\end{aligned} \tag{1}$$

The continuity equations take the following form:

$$\begin{aligned}\frac{\partial}{\partial t}(\rho_{\mathrm{l}}\alpha_{\mathrm{l}}) + \nabla\cdot(\rho_{\mathrm{l}}\alpha_{\mathrm{l}}\boldsymbol{u_l}) &= \Gamma_{\mathrm{lg}} \\ \frac{\partial}{\partial t}\left(\rho_{\mathrm{g}}\alpha_{\mathrm{g}}\right) + \nabla\cdot\left(\rho_{\mathrm{g}}\alpha_{\mathrm{g}}\boldsymbol{u_g}\right) &= -\Gamma_{\mathrm{lg}}\end{aligned} \tag{2}$$

where $\boldsymbol{u}$ is the velocity of each phase, p is the pressure, α represents the phase volume fraction, ρ is the density of each phase, Γ represents mass transfer rates, τ denotes the viscous stress tensor, τ^{T} denotes the Reynolds stress tensor, $\boldsymbol{g}$ is the vector of gravitational acceleration, $\boldsymbol{M}$ is the interfacial force and $\boldsymbol{F_V}$ denotes any other volume force term. Subscripts l and g denote liquid and gas phases, respectively. Subscript lg denotes transfer from liquid to gas and vice versa for subscript gl.

It must be mentioned that, in the above equations, the influence of surface tension in the case of liquid phase has been neglected and a single averaged bubble size has been adopted to neglect the effect of potential size distribution of the dispersed phase. The following equations represent the viscous stress tensor for Newtonian liquid and gas phases:

$$\begin{aligned}\tau_{\mathrm{l}} &= \mu_{\mathrm{l}}^{\mathrm{e}}\left(\nabla \boldsymbol{u_l} + \nabla \boldsymbol{u_l}^{\mathbf{T}} - \frac{2}{3}(\nabla \boldsymbol{u_l})\boldsymbol{I}\right)\\ \tau_{\mathrm{g}} &= \mu_{\mathrm{g}}^{\mathrm{e}}\left(\nabla \boldsymbol{u_g} + \nabla \boldsymbol{u_g}^{\mathbf{T}} - \frac{2}{3}(\nabla \boldsymbol{u_g})\boldsymbol{I}\right)\end{aligned} \tag{3}$$

where the effective viscosity μ^{e} is given as the sum of material viscosity, μ, and turbulent viscosity μ^{T}.

2.2 Energy balance equation

The classical energy conservation equation for two-phase flows results in two energy equations, one for each phase. While the total energy equation [10] takes into account the mechanical terms such as work done by the surface tension and effect of changes in mean curvature, it is often convenient to use the thermal energy formulation where the mechanical terms are insignificant compared to high heat transfer rates. The energy balance equations can then be written as follows [10]:

$$\begin{aligned}\frac{\partial}{\partial t}\left(\rho_{\mathrm{l}}\alpha_{\mathrm{l}}H_{\mathrm{l}}\right) + \nabla\cdot\left(\rho_{\mathrm{l}}\alpha_{\mathrm{l}}\boldsymbol{u_l}H_{\mathrm{l}}\right) &= \nabla\cdot\left[\alpha_{\mathrm{l}}\lambda_{\mathrm{l}}^{\mathrm{e}}\nabla T_{\mathrm{l}}\right] + \left(\Gamma_{\mathrm{lg}}H_{\mathrm{g}} - \Gamma_{\mathrm{gl}}H_{\mathrm{l}}\right) + Q_{\mathrm{l}}\\ \frac{\partial}{\partial t}\left(\rho_{\mathrm{g}}\alpha_{\mathrm{g}}H_{\mathrm{g}}\right) + \nabla\cdot\left(\rho_{\mathrm{g}}\alpha_{\mathrm{g}}\boldsymbol{u_g}H_{\mathrm{g}}\right) &= \nabla\cdot\left[\alpha_{\mathrm{g}}\lambda_{\mathrm{g}}^{\mathrm{e}}\nabla T_{\mathrm{g}}\right] + \left(\Gamma_{\mathrm{gl}}H_{\mathrm{l}} - \Gamma_{\mathrm{lg}}H_{\mathrm{g}}\right) + Q_{\mathrm{g}}\end{aligned} \tag{4}$$

where T denotes the temperature of each phase, λ^{e} is the effective thermal conductivity, H is the enthalpy and Q denotes the heat source density and can be given as the sum of the fission heat and the decay heat from DNPs, therefore directly coupling neutronics and thermal hydraulics.

In turbulent flows, the time smoothing of energy balance results in the appearance of a turbulent heat flux which can be expressed in terms of correlation of velocity and temperature fluctuations. The turbulent heat flux can be modelled using a number of empirical correlations, the most commonly used being the eddy thermal conductivity and the mixing length expressions of Prandtl and Taylor [12]. In the eddy conductivity approach, the turbulent flux is analogous to the Fourier law of heat conduction and is equal to $-\lambda^{\mathrm{T}}\nabla T$ where λ^{T} denotes the turbulent thermal conductivity given by the following equations:

$$\begin{aligned}\lambda^{\mathrm{T}} &= \frac{\mu^{\mathrm{T}}C_p}{\mathrm{Pr}^{\mathrm{T}}}\\ \mathrm{Pr}^{\mathrm{T}} &= \left(\frac{1}{\mathrm{Pr}_{\infty}^{\mathrm{T}}} + \frac{0.3}{\left(\mathrm{Pr}_{\infty}^{\mathrm{T}}\right)^{0.5}} - \left(\frac{0.3C_p\mu^{\mathrm{T}}}{\lambda}\left(1-\exp\left(-\frac{\lambda}{0.3C_p\mu^{\mathrm{T}}(\mathrm{Pr}_{\infty}^{\mathrm{T}})^{0.5}}\right)\right)\right)\right)^{-1}\end{aligned} \tag{5}$$

where μ^{T} and C_p denote the turbulent viscosity and heat capacity, respectively, and the turbulent Prandtl number, Pr^{T}, has been represented using the Kays–Crawford model [13] with the turbulent Prandtl number at infinity, $\mathrm{Pr}^{\mathrm{T}}_{\infty}$, equal to 0.85. Subsequently, the effective thermal conductivity, λ^{e}, can be expressed as the sum of material thermal conductivity, λ, and turbulent thermal conductivity, λ^{T}.

2.3 Bubbly flow model

While the equations discussed as part of the two-fluid model provide the most accurate results for all kinds of bubbly flows, their advantages are outweighed by the computational requirements. When this burden is not worth the effort, the equations for each phase can be combined into a single equation representative of both the phases. Such equations normally account for the flow in terms of the continuous phase and a gas-phase transport equation is added to track the volume fraction of the dispersed phase.

The bubbly flow model simulated in this work is a simplification of the Euler–Euler model discussed in the previous section. The bubbly flow model is based on the assumptions that the gas density is negligible compared to the liquid density, the motion of the gas bubbles relative to the liquid is determined by a balance between viscous drag and pressure forces, and the two phases share the same pressure field [6]. The momentum and the continuity equations for the two phases can then be combined, and a gas-phase transport equation can be added to keep track of the volume fraction of the gas bubbles. Furthermore, since the gas–liquid bubbly flows in MSFR do not involve any interfacial mass transfer, the mass transfer rates Γ_{lg} and Γ_{gl} are zero, resulting in the following system of equations [14]:

$$\alpha_{\mathrm{l}}\rho_{\mathrm{l}}\frac{\partial \boldsymbol{u_l}}{\partial t} + \alpha_{\mathrm{l}}\rho_{\mathrm{l}}\boldsymbol{u_l}\cdot\nabla\boldsymbol{u_l} = -\nabla p + \nabla\cdot\left[\alpha_{\mathrm{l}}(\mu_{\mathrm{l}}+\mu^{\mathrm{T}})\left(\nabla\boldsymbol{u_l} + \nabla\boldsymbol{u_l}^{\mathbf{T}} - \frac{2}{3}(\nabla\boldsymbol{u_l})\boldsymbol{I}\right)\right] + \alpha_{\mathrm{l}}\rho_{\mathrm{l}}\boldsymbol{g} + \boldsymbol{F} \tag{6}$$

$$\frac{\partial}{\partial t}\left(\rho_{\mathrm{l}}\alpha_{\mathrm{l}} + \rho_{\mathrm{g}}\alpha_{\mathrm{g}}\right) + \nabla\cdot\left(\rho_{\mathrm{l}}\alpha_{\mathrm{l}}\boldsymbol{u_l} + \rho_{\mathrm{g}}\alpha_{\mathrm{g}}\boldsymbol{u_g}\right) = 0 \tag{7}$$

where $\boldsymbol{u_l}$ is the velocity of liquid phase, p is the pressure, α denotes the phase volume fraction, ρ is the density, $\boldsymbol{g}$ is the gravity vector, $\boldsymbol{F}$ is any additional force per unit volume, μ_{l} denotes the dynamic viscosity of liquid and μ_T represents the turbulent viscosity.

For the case where there is no mass transfer between the two phases, the gas-phase transport equation can be written as:

$$\frac{\partial \rho_{\mathrm{g}}\alpha_{\mathrm{g}}}{\partial t} + \nabla\cdot(\rho_{\mathrm{g}}\alpha_{\mathrm{g}}\boldsymbol{u_g}) = 0 \tag{8}$$

Furthermore, at low void fractions, the role of bubbles in heat transfer is considered only through bubble-induced turbulence. The temperature field can be well approximated by the energy equation for liquids as follows:

$$\rho_{\mathrm{l}}c_P\frac{\partial T}{\partial t} + \rho_{\mathrm{l}}c_P\nabla\cdot(\boldsymbol{u_l}T) = \nabla\cdot\left[\lambda^{\mathrm{e}}_{\mathrm{l}}\nabla T\right] + Q \tag{9}$$

The power source density Q in the above equation couples the neutronics and the thermal hydraulics using the following equation [4]:

$$Q = (1-\beta)E_{\mathrm{f}}\Sigma_{\mathrm{f}}\Phi + \beta\lambda_{\mathrm{heat}}C \tag{10}$$

where E_f represents the energy produced per fission, Σ_f represents the macroscopic fission cross section, β represents the DNP fraction, λ_{heat} represents the decay heat constant, Φ represents the neutron flux and C represents the DNP concentration.

2.4 Neutronics

2.4.1 Neutron flux

An exact model for the neutronic analysis requires the complete neutron transport equation. In the literature, SP_3 neutron transport, multigroup neutron diffusion and Monte Carlo approaches have been explored for MSFR neutronics [5,15,16]. However, the one energy group neutron diffusion approximation [17], capable of capturing the complexity of coupled neutronic and thermal hydraulics in MSFR, has been adopted in this work to reduce the required computation time. The neutron diffusion equation takes the following form:

$$\frac{1}{v_n}\frac{\partial \Phi}{\partial t} = \nabla \cdot (D\nabla\Phi) - \Sigma_a\Phi + \lambda C + (1-\beta)\nu\Sigma_f\Phi \tag{11}$$

where Φ is the neutron flux, C denotes the delayed neutron precursor concentration, v_n is the average velocity of neutron population, Σ_a and Σ_f represent the macroscopic absorption and fission cross sections, respectively, D is the neutron diffusion coefficient, β is the fraction of fission neutrons emitted by precursors, ν is the average number of neutrons emitted per fission reaction and λ is the decay constant of the precursors. The macroscopic cross sections and their temperature dependencies can be calculated by means of Serpent Monte Carlo code [18] employing the JEFF-3.1 library [19].

The gas bubbles present in reactor core act as voids from the point of view of neutrons and have an impact on the nuclear data of MSFR fuel. The bubbles alter the effective volume of fuel and thereby alter the macroscopic cross sections. This effect can be accounted by weighting the cross section by the volume fraction of fuel.

$$\Sigma = \alpha_l\Sigma_l + \alpha_g\Sigma_g \approx \alpha_l\Sigma_l \tag{12}$$

Thermal feedback on neutronics has been accounted for by employing a simple logarithmic temperature dependence using cross sections at 900 K and 1200 K for the interpolation. The cross sections are assumed to be proportional to local density and also to local volume fraction of the fuel [20].

$$\begin{aligned}\Sigma(T,\rho,\alpha_l) &= \alpha_l\left(\frac{\rho}{\rho_0}\right)\left[\Sigma_0 + \alpha_\Sigma \log\left(\frac{T}{T_0}\right)\right]\\ D(T,\rho,\alpha_l) &= \frac{1}{\alpha_l}\left(\frac{\rho_0}{\rho}\right)\left[D_0 + \alpha_D \log\left(\frac{T}{T_0}\right)\right]\end{aligned} \tag{13}$$

where T_0 is the fuel reference temperature and ρ_0 is the fuel density at the reference temperature.

2.4.2 Delayed neutron precursor (DNP)

In the MSFR, the delayed neutron precursors drift along with the fuel salt. This DNP drift plays an important role in reactor dynamics of molten salt reactors and the equation for precursor concentration must account for the effect of fuel mobility. The velocity field of

the fuel is taken into account by introducing convection and diffusion terms in the balance equation of DNP [21–23] as shown below:

$$\frac{\partial C}{\partial t} + \boldsymbol{u_l} \cdot \nabla C - \nabla \cdot \left(\frac{\mu^{\mathrm{T}}}{\rho \mathrm{Sc}_T} \nabla C \right) = \beta \nu \Sigma_{\mathrm{f}} \Phi - \lambda C \tag{14}$$

where C is the precursor concentration, $\boldsymbol{u_l}$ is the fuel velocity, μ^{T} represents the turbulent viscosity and Sc is the turbulent Schmidt number which is equal to 0.85 [24,25].

2.5 Bubbling feedback coefficient

The effect of non-uniform neutronics perturbations can be estimated by a multigroup calculation where perturbations are represented by appropriate space-dependent group constants. However, such localised perturbations inherently require a multigroup calculation in at least two dimensions resulting in a high computational cost [26]. If the perturbations are not so large as to substantially distort the flux in the neighbourhood of the perturbation, *perturbation theory* can be employed to determine such effects. In case of small void fractions, the change in core multiplication caused by the bubbles is sufficiently small to be treated as a perturbation and therefore the original criticality calculation can be avoided [27].

The bubble-induced perturbations in the core parameters, as compared to single-phase flow, can be represented in terms of the gas void fraction as follows:

$$\begin{aligned} \delta \Sigma_{\mathrm{f}} &= -\alpha_{\mathrm{g}} \Sigma_{\mathrm{f}} \\ \delta \Sigma_{\mathrm{a}} &= -\alpha_{\mathrm{g}} \Sigma_{\mathrm{a}} \\ \delta D &= \frac{\alpha_{\mathrm{g}} D}{(1 - \alpha_{\mathrm{g}})} \end{aligned} \tag{15}$$

where α_{g} is the bubble void fraction computed from the gas-phase transport equation.

The reactivity change, based on the first-order perturbation theory, can be expressed as:

$$\Delta \rho = \frac{\int_{\Omega} \left[\Phi' \left(\nu \delta \Sigma_{\mathrm{f}} - \delta \Sigma_{\mathrm{f}} \right) \Phi - \nabla \Phi' \delta D \nabla \Phi \right] \mathrm{d}\Omega}{\nu \int_{\Omega} \Phi' \Sigma_{\mathrm{f}} \Phi \mathrm{d}\Omega} \tag{16}$$

where Φ' and Φ represent the perturbed and the unperturbed flux, respectively, and the domain Ω refers to the reactor core without the recirculation loops. The perturbed flux is associated with changes in macroscopic cross sections and diffusion length due to the effect of gas bubbles.

The reactivity feedback provided by the inert gas bubbles can be quantified in terms of the bubbling feedback coefficient. This coefficient is defined as the average reactivity inserted per unit of gas void fraction in the core and takes the following mathematical form:

$$\alpha_{\text{bubbling}} = \frac{\Delta \rho}{\frac{1}{\Omega} \int_{\Omega} \alpha_{\mathrm{g}} \mathrm{d}\Omega} \tag{17}$$

where the reactivity insertion due to bubbles $\Delta \rho$ can be computed by Eq. (16).

3 COMSOL multiphysics model

COMSOL Multiphysics is a finite element solver and multiphysics simulation software which is used for the solution of coupled systems of partial differential equations (PDEs). The predictive capabilities of COMSOL Multiphysics for MSFR modelling have previously been

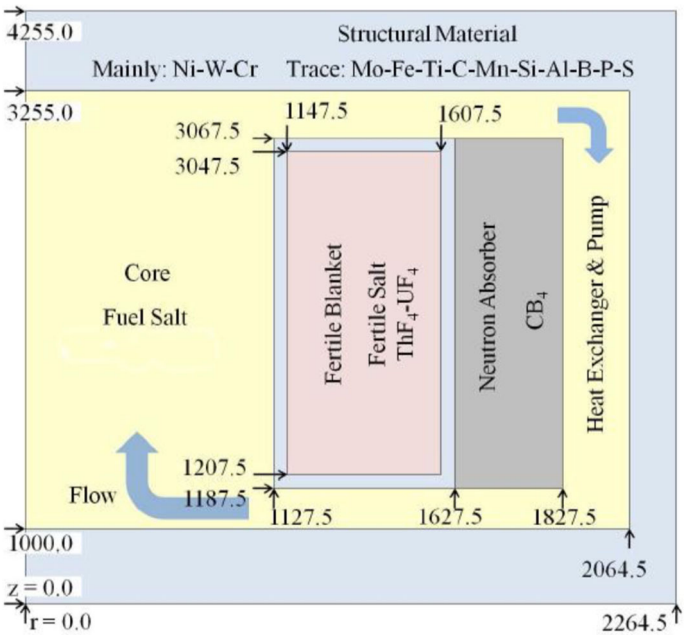

Fig. 1 Axially symmetric MSFR benchmark geometry [23]. The left boundary denotes the axis of the reactor

evaluated at Politecnico di Milano [28,29] and a number of models for MSFR have been developed using COMSOL [15,30]. While OpenFOAM has been widely used for multiphysics simulation of MSFR, in the present work COMSOL Multiphysics has been used with the aim of employing the finite element discretisation instead of the finite volume discretisation used in OpenFOAM. COMSOL allows accurate multiphysics modelling by offering well-defined coupling approaches and robust numerical methods allowing the user to focus on the physical and mathematical modelling of the phenomena. Using COMSOL made it possible for the work to be focused on exploring the applicability of the bubbly flow model to MSFR instead of focusing on implementing the model in OpenFOAM.

The conceptual design of MSFR proposed under the EVOL project consists of a cylindrical core geometry with 16 external loops for fuel re-circulation [31]. In the present work, this nearly axially symmetric core geometry has been extended to the complete primary circuit by approximating the 16 external re-circulation loops with a single annular loop. This modelling approach leads to drawbacks such as the impossibility to predict some localised effects in core such as the flow pattern in the vicinity of core inlet and outlet [15]. However, since the focus of the work is on the adoption of the bubbly flow model for MSFR, the simplified geometry is a reasonable modelling choice for the purpose of modelling assessment. In addition, it allows for a two-dimensional axially symmetric COMSOL model reducing computational costs and time required for the simulation. The model can be applied to the 3D toroidal geometry of MSFR at the later stages. The simplified benchmark geometry is illustrated in Fig. 1.

Though the two-dimensional model cannot explicitly represent the pumps and heat exchangers, replacing the physical components by volumetric forces and heat sources or sinks, respectively, serves as a good approximation. The pump has been simulated by a volume force in the direction of flow to establish a nominal fuel salt flow rate of 4.5 $m^3 s^{-1}$. The heat exchange with the intermediate circuit has been modelled using a heat sink proportional

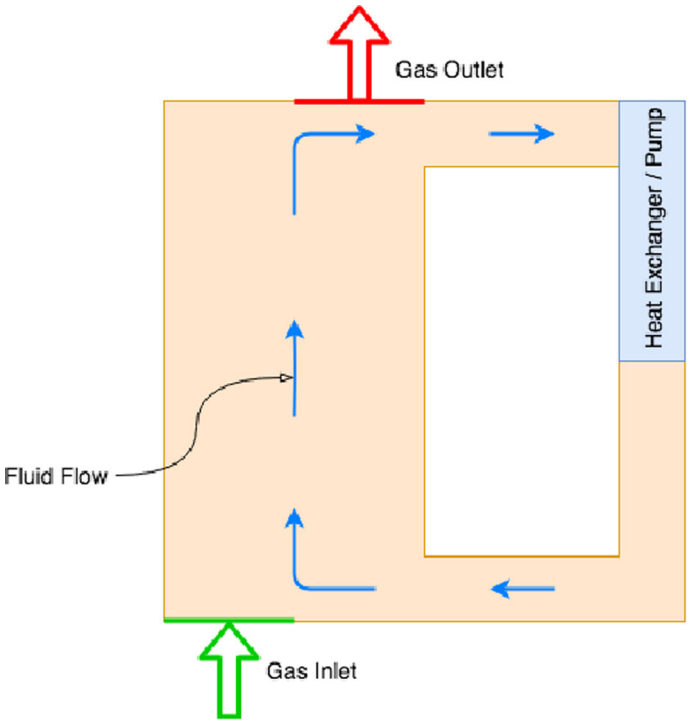

Fig. 2 Schematic description of the geometry used in the multiphysics model. The bubbles are injected through a distributed area at the base of the reactor, and the outlet is placed at the top of the core, close to the recirculation loop. The heat exchanger and pump marked in blue have been approximated by a volumetric heat source and a volumetric force, respectively

to the temperature difference between the primary and secondary circuits, and the heat transfer coefficient has been taken as the harmonic mean of the heat transfer coefficients on each side of heat exchanger [15]. Bubble inlet was defined at the bottom of the core near the centre of the core, and the outlet was defined at the top surface of the core close to re-circulation loop outlet, as shown in Fig. 2.

To achieve a good compromise between numerical accuracy and computational requirements, the mesh consists of triangular elements with progressive refinement close to the walls and bubble inlet and outlet. $\mathbb{P}2/\mathbb{P}1$ elements have been adopted for the fluid flow variables, namely velocity and pressure, while linear Lagrangian elements have been used for other variables, namely, temperature, neutron flux and delayed neutron precursor concentration. A segregated approach has been adopted using direct solver MUMPS [32,33] for the solution of each segregated group as shown in Fig. 3.

4 Results and discussion

4.1 Thermal hydraulics

The multiphysics model developed based on the equations presented in Sect. 2 was compared with a previous study performed by Fiorina et al. [34]. While a single-phase model was

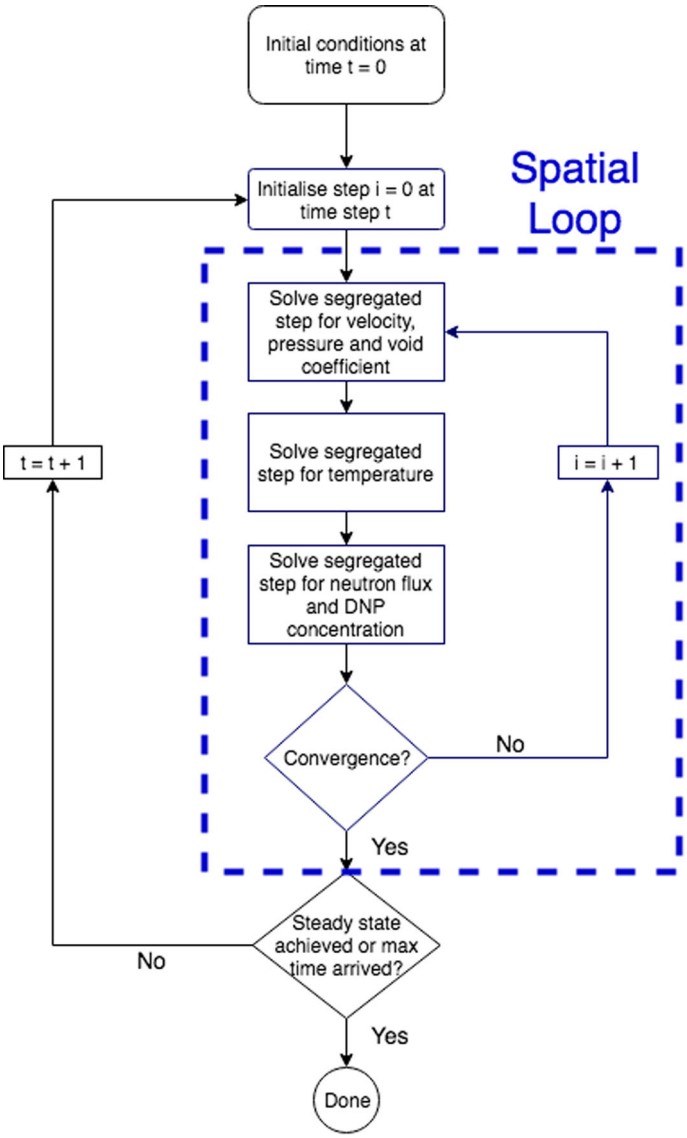

Fig. 3 Schematic diagram showing the segregated solver scheme adopted for the solution of the finite element multiphysics model in COMSOL

employed in [34], a zero void fraction was imposed in the present model for the sake of comparison. Though the results by Fiorina et al. are not shown for brevity, both the velocity and temperature fields obtained in this work follow the same distribution as the single-phase model. The close agreement of results with the results by Fiorina et al. serves as a simple verification of the multiphysics model. As shown in Fig. 4, a wide recirculation zone exists close to the blankets, while the fuel is nearly stagnating at the core centre, near the axial reflectors. This is a direct consequence of the benchmark geometry shape and the inertial motion of the fuel salt entering the reactor core from recirculation loop.

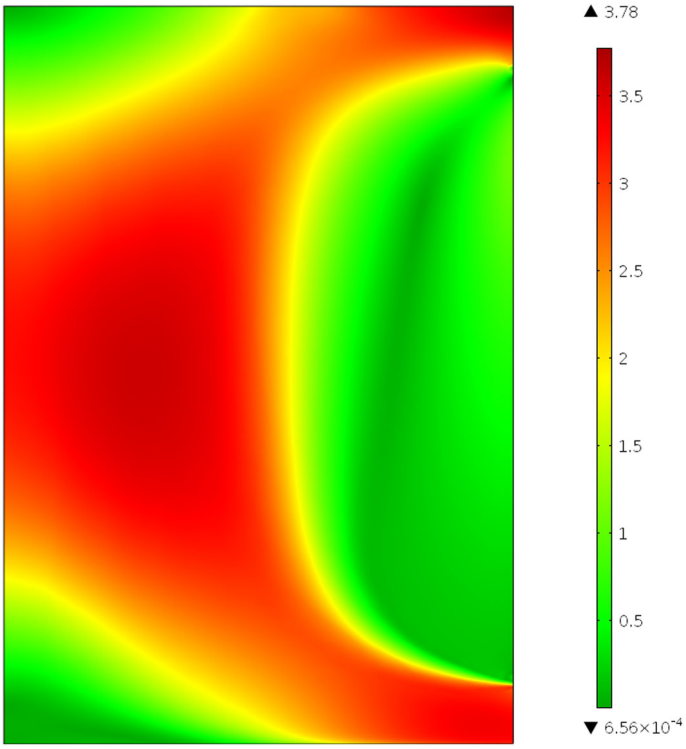

Fig. 4 Single-phase flow velocity field in the core (m s^{-1}) shows the presence of recirculation zone on the right and stagnation zones on the left bottom and top

Figure 5 shows the temperature distribution in the reactor core. The temperature in the recirculation zone is higher than the temperature at the outlet by around 300 K. This is due to the reduced heat removal as a consequence of reduced flow near the blanket. The reduced flow also causes a build-up of DNPs in the recirculation region and leading to an increase in the decay heat and contributing to the higher temperature in the region. Though the increased temperatures can lead to higher thermal stresses in the structural material, the problem has been resolved by employing an hourglass-shaped core under the SAMOFAR project [35]. However, since the present work focuses on the application of the developed model to predict the reactivity feedback of the bubbles, the simplified geometry has been employed.

A nominal bubbling mass flow rate of 20 ltr/sector/min has been prescribed under the SAMOFAR project. At this mass flow rate, the void distribution obtained in the reactor core is shown in Fig. 6. Due to the relatively large gas inlets and outlets used in this model, the bubbles collect close to the inlet an outlet. While a dragging effect on the bubbles as they enter the core should have carried them to the core, the fluid streamlines obtained in this geometry fail to accomplish this. Thus, the injection of bubbles close to the recirculation loop entry, as used by Cervi et al., proves to be a better choice.

In the case of two-phase flows, as a consequence of bubble-induced turbulence, a higher fuel salt velocity compared to single-phase flow has been observed. Figure 7 shows that even though the velocity field remains similar in shape to single-phase flow, the maxi-

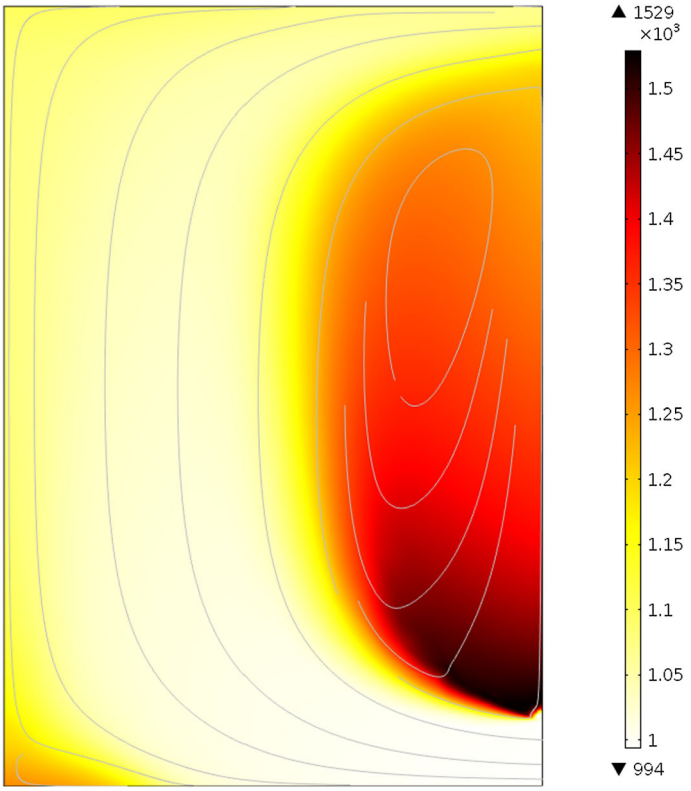

Fig. 5 Single-phase flow temperature distribution in the core (K) with superimposed velocity streamlines. The high temperatures in the recirculation zone are the result of reduced heat removal

mum velocity increases and the difference between the velocities in the two cases is shown in Fig. 8. However, a comparison of the temperature profile obtained from single-phase and two-phase studies reveals little difference in the simulated temperature profiles. This observation can be attributed to almost equal turbulent viscosity (and subsequently turbulent conductivity) achieved in the two cases. Turbulent viscosity depends on turbulent kinetic energy and dissipation rate predicted by the k–ϵ turbulence model. At small bubble void fractions, as in this work, the difference between turbulent kinetic energies and dissipation rates for the two cases is negligible resulting in almost identical turbulent viscosities. For the sake of brevity, the plot of these quantities has not been presented in the paper.

4.2 Neutronics

The theoretical axial distribution of the normalised neutron flux for a homogeneous reactor is expressed as $\cos(\pi z/H_e)$, where H_e is the effective height and z is the distance along the axis from the centre of the core [26]. For verification purposes, the normalised neutron flux calculated from the multiphysics model for MSFR was compared with the theoretical axial distribution, assuming a single-phase flow. Figure 9 shows the flux along

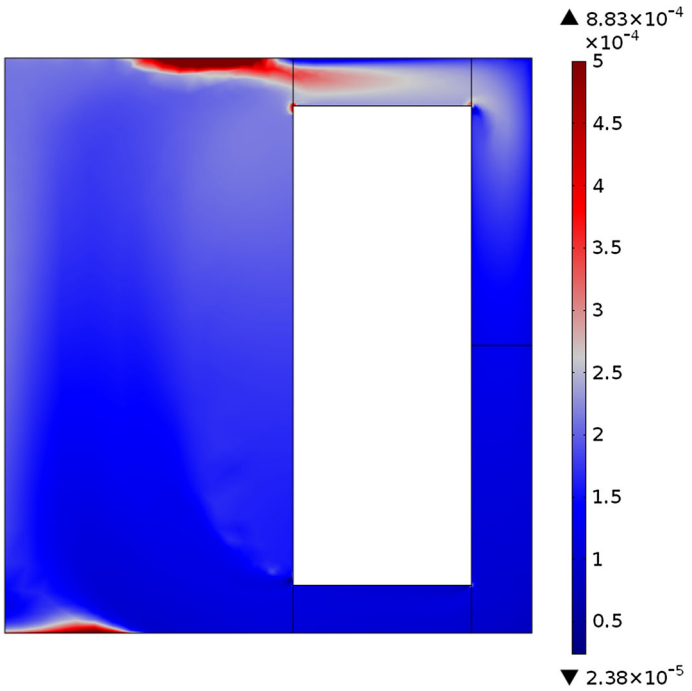

Fig. 6 Void distribution corresponding to nominal bubble flow rate shows that the bubbles accumulate close to the inlet and outlet. The void distribution is also higher in the recirculation and stagnation zones

the axial coordinate of MSFR computed through the multiphysics model with and without flow along with the theoretical flux. As is clear from Fig. 10, which shows the relative difference between the computed flux distributions and the theoretical one, the computed flux distributions closely resemble the theoretical. The agreement verifies the a priori assumption that the fuel salt motion does not significantly affect the neutron flux distribution.

The delayed neutron precursors, on the other hand, drift along with the fuel and show a higher concentration towards the top of the reactor. Moreover, the DNPs get transported to the recirculation loop and decay outside the core, leading to a reduction in the effective multiplication factor in the core. The spatial distributions of neutron flux and DNPs in MSFR, considering single-phase flow, are shown in Figs. 11 and 12. While a single DNP family has been modelled in this work, it can be conjectured that fluid flow has different impact on distributions of different precursors. In fact, the precursors with smaller decay constants (longer lifetime) flow further downstream compared to precursors with larger decay constants (shorter lifetime). Therefore, it can be concluded that the liquid-fuel flow has stronger effects on the precursors with longer lifetimes [34,36].

The bubbles, however, can have a significant influence on both neutron flux and DNPs. The bubbles affect both the effective macroscopic cross sections of the fuel salt as well as the spatial distribution of fuel salt in the core, thus impacting the neutron flux and DNP concentrations through both spatial and importance effects. However, in the present work, owing to the very low void fractions, the impact of the bubbles has been observed only to a very small extent. To avoid repeating figures which exhibit very similar results, the neutron

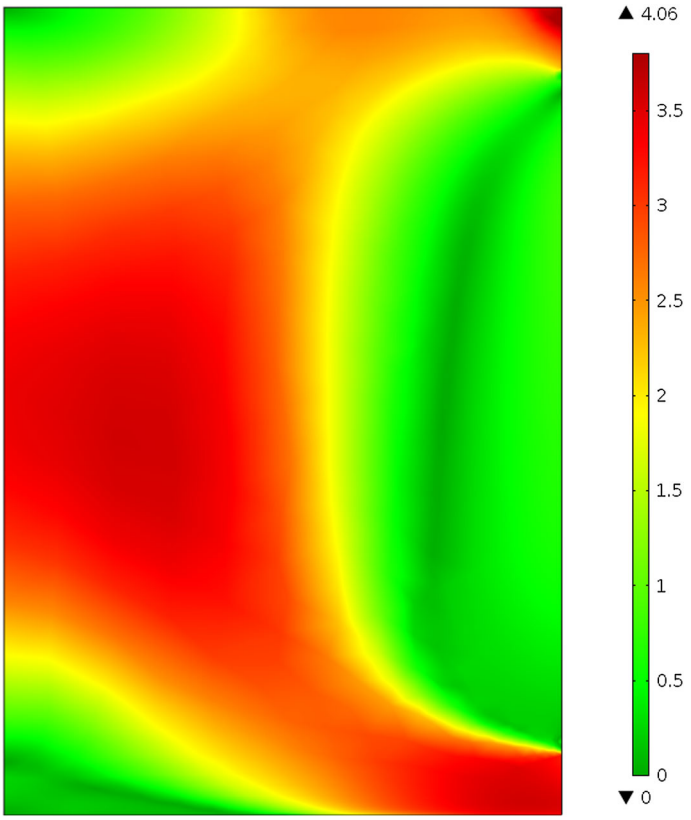

Fig. 7 Velocity field in core (m s^{-1}) in two-phase flow. The recirculation and stagnation zones are reduced in volume, and a larger area has a higher velocity near the centre of the core. However, the top left corner has a lower velocity due to accumulation of bubbles

flux and DNP concentration for bubbly flow have been omitted. Instead, to visualise the impact of bubbles, Fig. 13 shows the comparison between the computed normalised neutron flux distribution and the theoretical cosine-shaped distribution calculated with bubbly flow. The relative difference between the two distributions, shown in Fig. 14, exhibits the significant impact of the bubbles on the neutron flux distribution.

Figure 15 shows the spatial distribution of the difference in neutron fluxes for single-phase and two-phase flows, and Fig. 16 shows a similar distribution for DNPs. While the difference for neutron flux is highest at the places with highest void fractions, the difference for DNPs closely resembles the difference in velocity field. This behaviour further supports the inference that while neutron flux is only affected by the voids, the DNPs are affected by a combination of fluid flow and void effects.

The bubbles provide an additional transport mechanism for DNPs, some of which are constituted by metallic species that are not soluble in the molten fluoride matrix. These precursors may leave the fuel circuit due to extraction by gas bubbling or deposition in cold metallic surfaces in the out-of-core part of the loop [37]. This results in a reduction in the effective multiplication factor of the core as shown in Table 1.

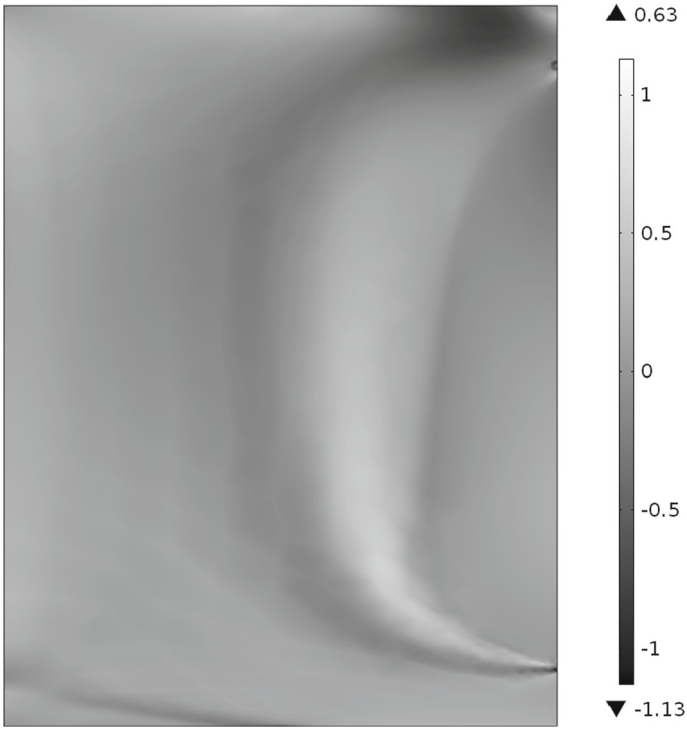

Fig. 8 Difference in liquid phase velocities for single and two-phase flows in core. The areas represented in lighter shades have a higher velocity in two-phase. However, due to accumulation of bubbles, a stagnation is observed close to the recirculation loop outlet

4.3 Bubbling feedback

The bubbling feedback coefficient was evaluated on the basis of the spatial distribution of the bubbles (shown in Fig. 6) using first-order perturbation theory, and the resulting coefficients were compared with those obtained by Brovchenko et al. using simulations performed with uniform void fractions [38]. At the nominal bubbling mass flow rate prescribed under the SAMOFAR project, that is 20 ltr/sector/min, the bubbles provide a negative reactivity insertion equal to -1.3104 pcm for an average void fraction equal to 1.3817×10^{-4}%. This corresponds to a bubbling feedback coefficient equal to -105.8514 pcm/% which is lower than the bubbling feedback obtained under SAMOFAR using Monte Carlo simulations. The difference in two predictions can mainly be attributed to the differences in the two modelling approaches. These differences include, but are not limited to, the one-group diffusion approximation and the use of volume-averaged methods in order to minimise the associated computational costs.

In order to better predict the impact of bubbles, computations for different mass flow rate of the gas were performed and the obtained results are reported in Table 2. Owing to the same inlet/outlet boundary conditions and flow, the spatial distribution of the bubbles for different mass flow rates was similar to the one shown in Fig. 6, and while only a tiny change was observed in the bubbling feedback coefficient corresponding to different mass flow rates, a further comparison with the uniform void fraction study by Brovechenko et al. [38] and another study by Cervi et al. [39] demonstrates the dependence of the bubbling feedback

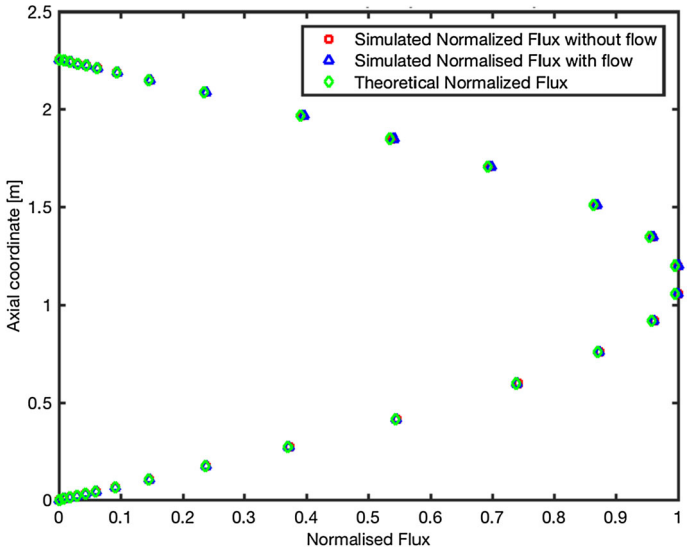

Fig. 9 Comparison of normalised neutron flux distribution along the axis (i.e. $r = 0$ in the axisymmetric model) in the case of single-phase flow. The flow is expected to have negligible impact on the distribution, and the computed distribution for both flow and no-flow case closely matches the theoretical cosine-shaped axial distribution

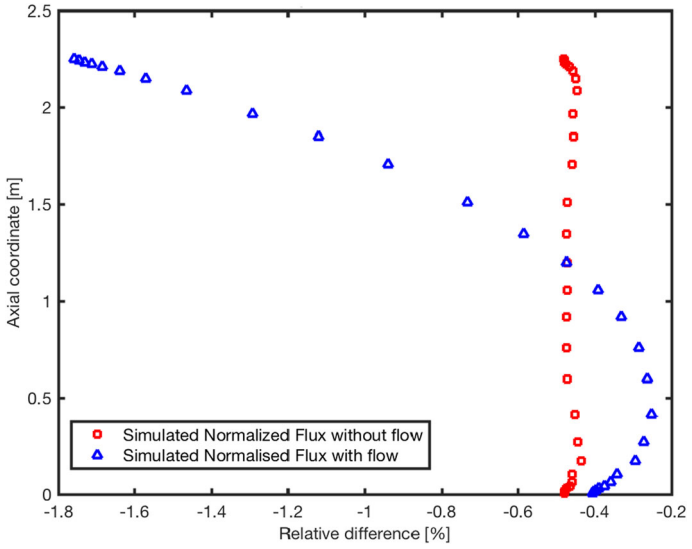

Fig. 10 Relative difference of the computed neutron flux distributions with respect to the theoretical cosine-shaped distribution. For the case without flow, the difference is around 0.5%, while for the case with flow the difference is slightly higher close to the top of the core but is still relatively small

coefficient on the gas bubble distribution within the core. In fact, the results by Cervi et al. [39] show a significant difference in the values of bubbling feedback coefficient for different void fractions as opposed to the present work. This discrepancy arises from the difference in bubble inlet and outlet boundaries. While Cervi et al. considered the bubble inlet as an

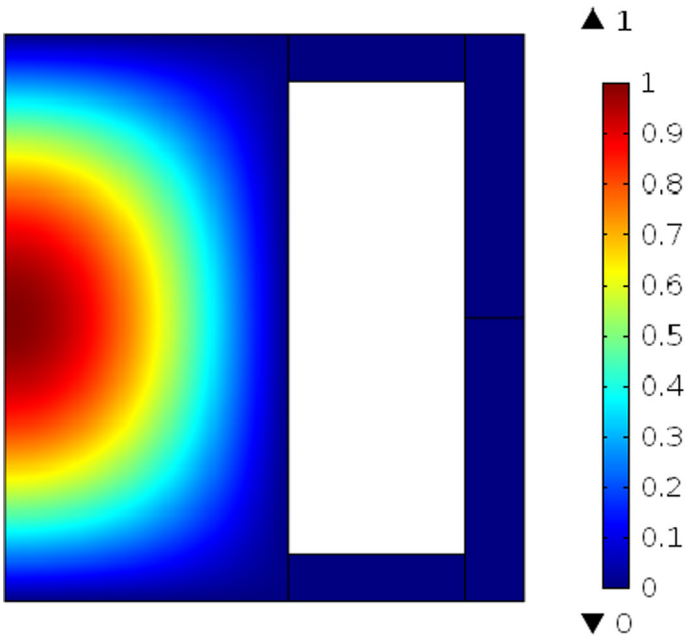

Fig. 11 The normalised neutron flux in MSFR for the case without bubbles

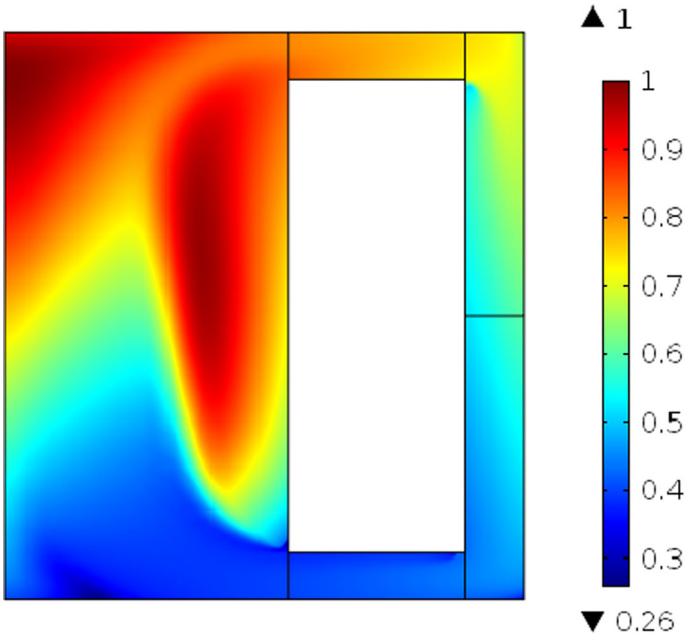

Fig. 12 Normalised DNP distribution in MSFR shows that drift of the DNPs along with the fuel salt. As a result, the DNPs collect towards the top and also flow out of the core into the recirculation loops. A higher concentration of DNPs in the recirculation and stagnation zone is observed

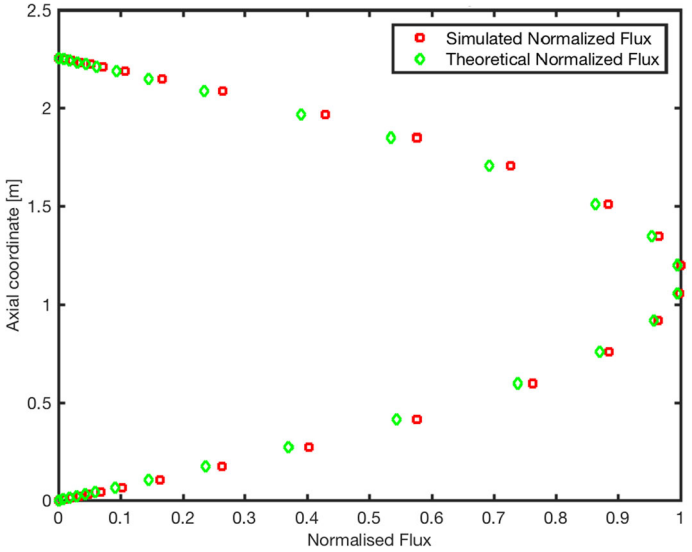

Fig. 13 Normalised neutron flux distribution along the axis (i.e. $r = 0$ in the axisymmetric model) for bubbly flow

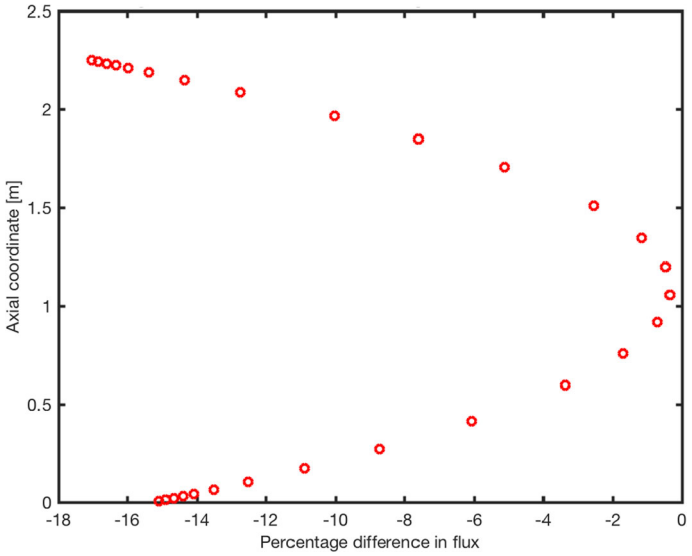

Fig. 14 Relative difference between computed and theoretical normalised neutron flux distribution along the axis shows that while the fuel salt flow had little impact on the distribution, the bubbles have a relatively much prominent impact

injection and the outlet as a suction, resulting in the bubbles being concentrated in a smooth streamline close to the centre of the core, distributed inlet and outlet were considered in this work, resulting in accumulation of bubbles in areas of low neutronic importance. Moreover, such an accumulation also contributes to comparatively lower bubbling feedback coefficient as mentioned before. Furthermore, for very small void fractions, as in the present case, the

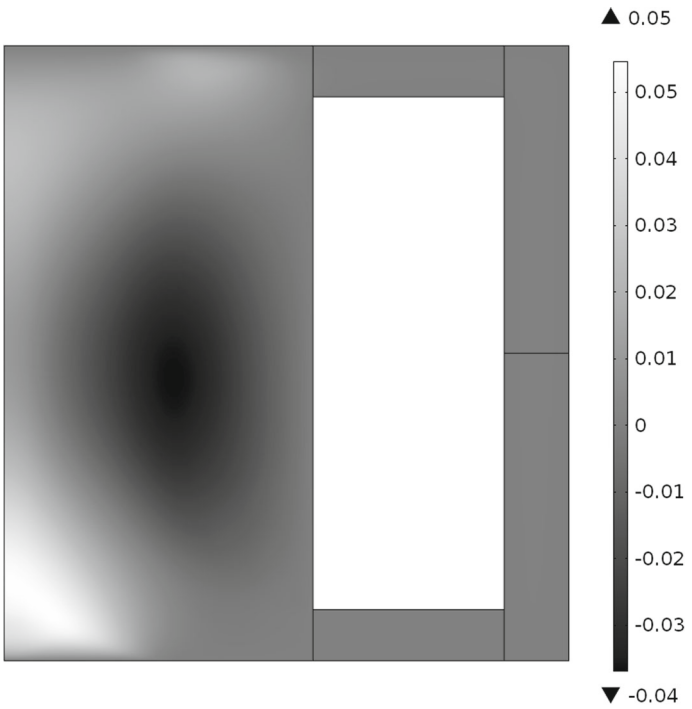

Fig. 15 Difference between neutron flux for flows with and without bubbles shows that the highest effect is close to the top and bottom and near the axis. This corresponds to the bubble distribution shown in Fig. 6

distribution remains relatively unaffected for different void fractions, thus contributing to the predicted values of α_{bubbling}.

5 Conclusions

Owing to its several favourable characteristics with respect to GEN- IV solid-fuelled reactors, such as the presence of strong negative void and temperature feedbacks and a low fissile inventory, Molten Salt Fast Reactor has garnered significant scientific and industrial interest. However, the strong coupling between fluid flow, heat transfer and neutronics makes modelling and simulation of MSFR a challenging task. This is even more complex if we consider the bubbling system which makes the fuel salt a two-phase mixture. In this paper, an effort has been made to develop a multiphysics model to predict the impact of the inert gas bubbles on the thermal hydraulics and neutronics of the MSFR.

In particular, the focus has been on coupling the bubbly flow model for dispersed two-phase flow at low void fractions with heat transport equation and neutronics model consisting of one-group neutron diffusion equation and DNP transport equation to develop a multiphysics model to predict the void feedback coefficient of the inert gas bubbles. A multiphysics model developed using COMSOL has been used to simulate the steady-state behaviour of the MSFR, and for the simplified cylindrical geometry employed in the present work, it was shown that the bubble-induced turbulence leads to an increase in the salt velocity although the temperature field was relatively unchanged at very small void fractions. Neutronics results show that both

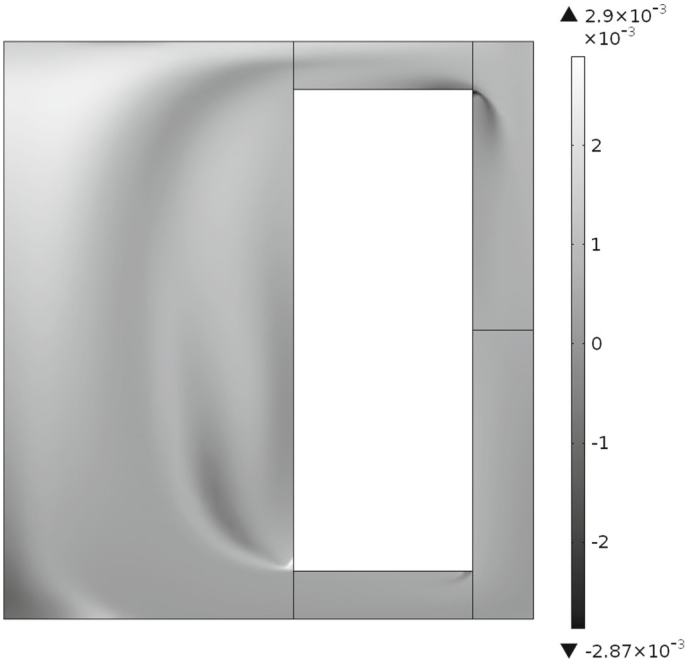

Fig. 16 Difference in concentration of DNPs for flows with and without bubbles closely resembles the difference in liquid phase velocities for flows with and without bubbles as shown in Fig. 8

Table 1 Multiplication factors for different types of fuel flow

Non-circulating fuel	Single-phase circulating fuel	Two-phase circulating fuel
0.9802	0.9781	0.9669

the neutron flux and DNP concentration were affected by the gas bubbles and an average reactivity feedback coefficient of − 105.8514 pcm/% was obtained. An observation was the importance of spatial distribution of bubbles on the reactivity feedback provided, which was made evident by the difference in the bubbling feedback coefficient compared to the values obtained by previous studies that used a homogeneous distribution. However, better results can be expected by modelling the bubble inlet and outlets as a narrow aperture and moving the bubble inlet closer to the recirculation loop.

In future, the model will be improved by adopting a multigroup diffusion approximation and using an adjoint perturbation analysis to predict the spatial importance of the inert gas bubbles. Furthermore, since the fuel salt–gas mixture can be highly compressible with low speed of sound, compressibility effects will be included in this model. Cervi et al. [4] have investigated the impact of the fuel mixture compressibility during accidental super-prompt-critical scenarios, using the Euler–Euler model. Including these effects in the simplified bubbly flow model used in this work can be particularly useful for applications such as control-oriented models of MSFR where the full fidelity Euler–Euler model might be computationally expensive.

Table 2 Reactivity change versus average core void fraction

Void fraction (%)	Multiplication factor	Void coefficient (pcm/%)
0.00	0.979900	
0.69×10^{-4}	0.979880	– 105.61
1.38×10^{-4}	0.979875	– 105.78
1.72×10^{-4}	0.979869	– 105.77
2.07×10^{-4}	0.979862	– 106.46
2.76×10^{-4}	0.979849	– 105.74
3.44×10^{-4}	0.979837	– 105.72

References

1. SAMOFAR.EU. About SAMOFAR. Available at http://samofar.eu/. Accessed May 24, 2019
2. D. Gèrardin, M. Allibert, D. Heuer, A. Laureau, E. Merle, C. Seuvre, in *Proceedings of International Conference on Fast Reactors and Related Fuel Cycles: Next Generation Nuclear Systems for Sustainable Development (FR17)* (Yekaterinburg, Russia, 2017)
3. J. Serp, M. Allibert, O. Beneš, S. Delpech, O. Feynberg, V. Ghetta, D. Heuer, D. Holcomb, V. Ignatiev, J.L. Kloosterman, L. Luzzi, E. Merle-Lucotte, J. Uhlíř, R. Yoshioka, D. Zhimin, Prog Nuclear Energy **77**, 308 (2014). https://doi.org/10.1016/j.pnucene.2014.02.014
4. E. Cervi, S. Lorenzi, A. Cammi, L. Luzzi, Chem. Eng. Sci. **193**, 379 (2019). https://doi.org/10.1016/j.ces.2018.09.025
5. E. Cervi, S. Lorenzi, L. Luzzi, A. Cammi, Ann. Nuclear Energy **132**, 227 (2019). https://doi.org/10.1016/j.anucene.2019.04.029
6. A. Sokolichin, G. Eigenberger, A. Lapin, AIChE J. **50**(1), 24 (2004). https://doi.org/10.1002/aic.10003
7. G.B. Wallis, *One-Dimensional Two-Phase Flow* (McGraw-Hill, New York, 1969)
8. M. Ishii, *Thermo-fluid dynamic theory of two-phase flow*. No. 22 in Collection de la Direction des Etudes et Recherches d'Electricite de France (Eyrolles, Paris, 1975)
9. R. Lahey Jr., D. Drew, Chem. Eng. Commun. **118**(1), 125 (1992). https://doi.org/10.1080/00986449208936090
10. M. Ishii, T. Hibiki, *Thermo-Fluid Dynamics of Two-Phase Flow*, 1st edn. (Springer, New York, 2006)
11. H. Rusche, Computational fluid dynamics of dispersed two-phase flows at high phase fractions. Ph.D. thesis, Imperial College London, London, United Kingdom (2003)
12. R. Bird, W. Stewart, E. Lightfoot, *Transport Phenomena*, Revised 2 edn. (Wiley, New York, 2007)
13. W.M. Kays, M.E. Crawford, *Convective Heat and Mass Transfer*, 3rd edn. (McGraw-Hill, Boston, 1993)
14. D. Kuzmin, S. Turek, *Efficient Numerical Techniques for Flow Simulation in Bubble Column Reactors* (Univ. Dortmund, Fachbereich Mathematik, 2000)
15. C. Fiorina, A. Cammi, L. Luzzi, K. Mikityuk, H. Ninokata, M.E. Ricotti, J. Phys. Conf. Ser. **501**(1), 012030 (2014). https://doi.org/10.1088/1742-6596/501/1/012030
16. E. Cervi, S. Lorenzi, A. Cammi, L. Luzzi, Nuclear Eng. Design **346**, 209 (2019). https://doi.org/10.1016/j.nucengdes.2019.03
17. J.J. Duderstadt, L.J. Hamilton, *Nuclear Reactor Analysis* (Wiley, New York, 1976)
18. J. Leppänen, M. Pusa, T. Viitanen, V. Valtavirta, T. Kaltiaisenaho, Ann. Nuclear Energy **82**, 142 (2015). https://doi.org/10.1016/j.anucene.2014.08.024. Joint International Conference on Supercomputing in Nuclear Applications and Monte Carlo 2013, SNA + MC 2013. Pluri- and Trans-disciplinarity, Towards New Modeling and Numerical Simulation Paradigms
19. A. Koning, R. Forrest, M. Kellett, R. Mills, H. Henriksson, Y. Rugama, O. Bersillon, O. Bouland, A. Courcelle, M.C. Duijvestijn, E. Dupont, J. Kopecky, D. Leichtle, F. Marie, M. Mattes, E. Menapace, B. Morillon, C. Mounier, G. Noguerre, P. Pereslavtsev, P. Romain, O. Serot, S. Simakov, S. Tagesen, H. Vonach, P. Batistoni, P. Bem, F. Gunsing, M. Pillon, A. Plompen, P. Rullhusen, K. Seidel, M. Avrigeanu, V. Avrigeanu, E. Bauge, H. Leeb, M.J. Lopez Jimenez, D. Bernard, A. Bidaud, R. Dagan, C. Dean, P. Dos-Santos-Uzarralde, U. Fischer, A. Hogenbirk, R. Jacqmin, C. Jouanne, I. Kodeli, J. Leppanen, S.C.v.d. Marck, R. Perel, R. Perry, M. Pescarini, A. Santamarina, J.C. Sublet, A. Trkov, M.M. Be, T.D. Huynh, M. Kellett, R. Mills, A. Nichols, H. Henriksson, C. Nordborg, A. Nouri, Y. Rugama, E. Sartori, The JEFF-3.1 nuclear

data library. Tech. Rep. NEA–6190, Organisation for Economic Co-Operation and Development, Nuclear Energy Agency - OECD/NEA, Issy-les-Moulineaux (2006)
20. C. Fiorina, M. Aufiero, A. Cammi, C. Guerrieri, J. Krepel, L. Luzzi, K. Mikityuk, M.E. Ricotti, in *Proceedings of International Conference On Nuclear Engineering (ICONE)* (Anaheim, USA, 2012)
21. A. Cammi, V. Di Marcello, L. Luzzi, V. Memoli, M.E. Ricotti, Ann. Nuclear Energy **38**(6), 1356 (2011). https://doi.org/10.1016/j.anucene.2011.01.037
22. A. Cammi, C. Fiorina, C. Guerrieri, L. Luzzi, Nucl. Eng. Design **246**, 12 (2012). https://doi.org/10.1016/j.nucengdes.2011.08.002. Selected and expanded papers from International Conference Nuclear Energy for New Europe 2010, Portoroz, Slovenia, September 6–9, 2010
23. E. van der Linden, Coupled neutronics and computational fluid dynamics for the molten salt fast reactor. Master's thesis, Technical University of Delft, Delft, Netherlands (2012)
24. L.Y. Jiang, I. Campbell, Int. J. Heat Mass Transf. **51**(5), 1251 (2008). https://doi.org/10.1016/j.ijheatmasstransfer.2007.12.006
25. Y. Tominaga, T. Stathopoulos, Atmos. Environ. **41**(37), 8091 (2007). https://doi.org/10.1016/j.atmosenv.2007.06.054
26. J. Lamarsh, *Introduction to Nuclear Reactor Theory*, 1st edn. (Addison-Wesley Pub. Co., New York, 1966)
27. D.G. Cacuci, *Sensitivity and Uncertainty Analysis. Theory*, vol. 1 (Chapman and Hall/CRC, New York, 2003)
28. A. Cammi, V. Di Marcello, C. Fiorina, L. Luzzi, in *Proceedings of COMSOL Conference* (Boston, USA, 2009)
29. C. Fiorina, A generalized approach to assess the COMSOL capabilities for the analysis of the MSR thermo-fluid dynamics. Master's thesis, Politecnico di Milano, Milan, Italy (2009)
30. M. Zanetti, Development of new tools for the analysis and simulation of circulating-fuel reactor power plants. Ph.D. thesis, Politecnico di Milano, Milan, Italy (2016)
31. E. Merle-Lucotte, D. Heuer, M. Allibert, M. Brovchenko, N. Capellan, V. Ghetta, in *Proceedings of ICAPP 2011* (Nice, France, 2011)
32. P.R. Amestoy, I.S. Duff, J. Koster, J.Y. L'Excellent, SIAM J. Matrix Anal. Appl. **23**(1), 15 (2001). https://doi.org/10.1137/S0895479899358194
33. P.R. Amestoy, A. Guermouche, J.Y. L'Excellent, S. Pralet, Parallel Comput. **32**(2), 136 (2006). https://doi.org/10.1016/j.parco.2005.07.004
34. C. Fiorina, The Molten Salt Fast Reactor as a fast spectrum candidate for Thorium implementation. Ph.D. thesis, Politecnico di Milano, Milan, Italy (2013)
35. H. Rouch, O. Geoffroy, P. Rubiolo, A. Laureau, M. Brovchenko, D. Heuer, E. Merle-Lucotte, Ann. Nuclear Energy **64**, 449 (2014). https://doi.org/10.1016/j.anucene.2013.09.012
36. A. Laureau, P.R. Rubiolo, D. Heuer, E. Merle-Lucotte, M. Brovchenko, in *Proceedings of Joint International Conference on Supercomputing in Nuclear Applications + Monte Carlo* (2014)
37. X. Doligez, Fuel salt reprocessing influence on the MSFR behavior and on its associated reprocessing unit. Ph.D. thesis, Institut National Polytechnique de Grenoble - INPG, Grenoble, France (2010)
38. M. Brovchenko, D. Heuer, E. Merle-Lucotte, M. Allibert, V. Ghetta, A. Laureau, P. Rubiolo, Nuclear Sci. Eng. **175**(3), 329 (2013). https://doi.org/10.13182/NSE12-70
39. E. Cervi, S. Lorenzi, A. Cammi, L. Luzzi, in *Proceedings of International Conference Nuclear Energy for New Europe* (Bled, Slovenia, 2017)